ELSEVIER

Cement & Concrete Composites 23 (2001) 313–330

Cement & Concrete Composites

www.elsevier.com/locate/cemconcomp

On the ability of a class of random models to portray the structural features of real, observed, porous media in relation to fluid flow

Yannick Anguy [a,*], Robert Ehrlich [b], Azita Ahmadi [a], Michel Quintard [c]

[a] *Laboratoire Energétique et Phénomènes de Transfert, UMR CNRS No 8508, Esplanade des Arts et Métiers, 33405 Talence Cedex, France*
[b] *Residuum Energy, 1048 S. Oak Hills Way, Salt Lake City, UT 84108, USA*
[c] *Institut de Mécanique des Fluides de Toulouse, allée du Professeur Camille Soula, 31400 Toulouse, France*

The authors dedicate their work to the memory of their friends, John Barclay FERM and John C. FERM.

Abstract

The description of transport processes is practically accomplished at the macroscopic scale compatible with our ability to observe, and measure processes. The macroscopic description requires to faithfully account for the effects of the detailed inter-phase boundaries on the microscopic level (the micro-structure) in the expression for macroscopic transport coefficients such as permeability. Herein, the porous descriptors held to express macroscopic coefficients are the porosity and the autocorrelation function (ACF) measured directly on a 2-D finite digital image of the porous material. The flow-relevance of the selected porous descriptors will be eventually demonstrated if synthetic porous media generated through a random model from measured porosity and ACF yield the same transport properties than the actual media. Towards that goal, synthetic 2-D numerical porous micro-structures are generated from measured porosity and ACF on two types of natural mechanical aggregates: an Upper Shoreface and a Tidal Channel Sandstone. The achieved synthetic porous media are shown to include all the geometrical features of the real, observed, natural aggregates. Such agreement between synthetic and actual media is demonstrated to be the consequence of: (1) the richness of the structural information carried out by the ACF and, (2) a structural noise produced by the "practical use" of the random model. The requirement to account for the impact on macroscopic physics of this structural noise is emphasized. Extension of the approach to artificial aggregates such as cement, mortars or concrete is shown to be a promising avenue.

Keywords: Porous micro-structure; 2-D digital images; Random stationary model; Autocorrelation function; Fourier transform analysis; Natural and artificial mechanical aggregates; Permeability

1. General context

Cement and mortar represent materials that are complex from many standpoints. These products are at first mechanical mixtures of dry ingredients with each ingredient differing in composition, shape and grain size. The addition of fluid (commonly water) adds a new phase that both occupies pore space and reacts with some of the solids. The mechanical process of mixing the dry material with the liquid imposes a fabric whose arrangement is sensitive to the method of mixing and the duration of mixing. Reactions between solids and liquids occur within this fabric with the production of gels that will entirely or partially crystallize. Knowledge of the chemical reactions, the ratios of solids and of liquids are insufficient to predict the short and long term physical properties of the final product. Prediction, therefore, requires the addition of a "fabric term" that quantifies the three-dimensional arrangement of the solid, liquid, gel, and crystal system.

These industrial products have their analogues in sedimentary rocks. In fact some rocks are to all intents and purposes natural mortar or cement. Physical properties of these natural materials are just as important to civil engineers and petroleum engineers as the properties of the artificial counterparts to their respective specialists. These properties, including permeability, effective diffusion, dispersion are the sum of uncountable events that are described in the microscopic flow and transport equations. The evolution of these properties as a func-

* Corresponding author. Tel.: +33-5-56-84-54-18; fax: +33-5-56-84-54-01.
E-mail address: yannick@lept-ensam.u-bordeaux.fr (Y. Anguy).

0958-9465/01/$ - see front matter
PII: S0958-9465(00)00082-2

Nomenclature

$A_{\beta\sigma}$ interfacial area of the β–σ interface associated with the closure problem [24], m^2 (Eqs. (3))

$\underset{\sim}{d}$ closure vector field, m (Eqs. (3)). The closure variable d is related to the microscopic spatial deviation pressure $\dot{p}_\beta$ according to: $\dot{p}_\beta = d \cdot (\nabla\langle p_\beta\rangle^\beta - \rho_\beta g)$ [24,27,28]. The spatial deviation pressure $\dot{p}_\beta$ is defined according to Gray's [29] decomposition of length-scales: $p_\beta = \langle p_\beta\rangle^\beta + \dot{p}_\beta$

$\underset{\approx}{D}$ closure second-order tensor field, m^2 (Eqs. (3)). The closure variable D is related to the microscopic velocity $\underset{\sim\beta}{v}$ according to $\underset{\sim\beta}{v} = (1/\mu_\beta)\underset{\approx}{D} \cdot (\nabla\langle p_\beta\rangle^\beta - \rho_\beta g)$ [24,27,28]

g gravity vector, m s^{-2}

$\mathcal{I}$ unit tensor

$\tilde{\tilde{K}}$ Darcy's law permeability tensor, m^2

$\tilde{\ell}_i$ lattice vector for the unit cell, m

l_β characteristic length-scale for the β-phase at the microscopic scale, m

l_σ characteristic length-scale for the σ-phase at the microscopic scale, m

L generic characteristic length-scale for averaged variables, m [23]

p_β microscopic pressure in the β-phase, N m^{-2}

$\langle p_\beta\rangle^\beta$ intrinsic volume averaged pressure, N m^{-2}, define as [22]: $\langle p_\beta\rangle^\beta|_x = (1/V_\beta)\int_{V_\beta(\underset{\sim}{x})} p_\beta(\underset{\sim}{x}+\underset{\sim\beta}{y})\,\mathrm{d}V_y$

$\underset{\sim}{r}$ position vector, m

$\tilde{r}_m$ characteristic length of the averaging volume (REV), m

$\underset{\sim\beta}{r}$ position vector locating points in the β-phase, m

$\underset{\sim\beta}{v}$ microscopic velocity vector in the β-phase, m s^{-1}

$\langle \underset{\sim\beta}{v}\rangle$ superficial volume averaged velocity, m s^{-1}, defined as [22]: $\langle \underset{\sim\beta}{v}\rangle|_x = (1/V)\int_{V_\beta(\underset{\sim}{x})} \underset{\sim\beta}{v}(\underset{\sim}{x}+\underset{\sim\beta}{y})\,\mathrm{d}V_y$

V volume of the averaging volume, m^3

V_β volume of the β-phase contained in the averaging volume, m^3

$\underset{\sim}{x}$ position vector locating the centroid of the averaging volume, m [22]

$\underset{\sim\beta}{y}$ position vector locating points in the β-phase relative to the centroid, m [22]

Greeks

ε porosity

μ_β dynamic viscosity of the β-phase, N s m^{-2}

ρ_β mass density of the β-phase, kg m^{-3}

Subscripts

β fluid phase

σ solid phase

tion of time t and/or the spatial coordinates, is strongly coupled to the evolution of the fabric as crystallization and recrystallization proceeds on the microscopic level.

The boundary problems allowing in principle the detailed description of transport and flow phenomena at the microscopic scale are well known [1]. Nonetheless, this refined analysis is impractical, essentially because the detailed geometry of the inter-phase surface boundaries, e.g., the fluid–solid interface, is not known and/or is far too complex to describe [1–6]. Therefore, from the practical point of view, a macroscopic level of description is conveniently introduced that is compatible with our ability to observe the medium [1]. At the macroscopic level, the actual discrete and discontinuous medium consisting of two, or more phases, is replaced by a fictitious medium in which every phase (e.g., solid phase, fluid phase(s)) is modeled as a continuum filling up the entire domain [1,2,4,7,8]. At the macroscopic level, knowledge of the detailed configuration of the microscopic interphase boundaries is no longer needed. Yet, the effects of the microscopic interfaces configuration are still present at the macroscopic level as expressed by macroscopic transport coefficients such as permeability [1–3,7,9–11]. In this respect, a comprehensive study of the relation between transport coefficients and the underlying micro-structure is a fundamental step towards predicting the short term and long term evolution of real and/or artificial porous media.

Over the past 15 years considerable progress has been made in sedimentary petrography in collecting fabric-structural information – i.e. porous descriptors noted $\mathcal{H}^i_{i=1,\mathcal{N}}$ – via image analysis that can be easily linked to physical data. The imager analytical data can be used to document the effect that the configuration of the solid matrix has on the properties where all other factors are held constant. Another use is to generate synthetic media that faithfully reflect the image-analyzed medium in such a way to model physical process from first principles. In this paper we provide the background for understanding the theory and rigor that such an analysis promises. Results on real media as well as from model media have been very promising in understanding the relationship between the structure of natural porous media and physical properties. Thus, there is hope that this approach may bear useful insights into the more complex problem of cements and mortars.

Our approach is based on "the change of scale method" that can be expressed in a number of ways: the stochastic approach [12], the homogenization theory [13], the Brownian approach [14], the variational approach [15] and the volume averaging technique [16–24]. We concentrate on the volume averaging technique. This technique when applied for example to the process of single phase flow through a rigid porous medium leads from the microscopic STOKES equations, describing what happens at each "mathematical point"

within the considered fluid phase, to the macroscopic DARCY's law (Eq. (1)) spatially averaged over some Elementary Volume (EV)

$$\langle \underset{\sim}{v} \rangle_{\beta} = -\frac{1}{\mu_\beta} \underset{\approx}{K}.(\underset{\sim}{\nabla} \langle p_\beta \rangle^{\beta} - \rho_\beta \underset{\sim}{g}), \tag{1}$$

where $\langle \underset{\sim}{v} \rangle_{\beta}$ and $\langle p_\beta \rangle^{\beta}$ are the superficial volume averaged velocity [22] and intrinsic volume averaged pressure [22], the state variables of relevance to a macroscopic description.

In the rigorous smoothing process leading to Eq. (1), the size r_m of the averaging volume is constrained by the length-scale constraints expressed by Eq. (2) and satisfied by a variety of systems of practical importance [20]

$$l_\beta, l_\sigma \ll r_m \ll L, \tag{2}$$

where l_β, l_σ are characteristic length-scales for the fluid phase (β) (e.g., mean pore size), and the solid phase (σ) (e.g., mean grain size) on the microscopic scale. The left-hand side of Eq. (2) refers to the requirement that a geometrical Representative Elementary Volume (REV) exists. That is, that the size r_m of the averaging volume must be large enough to smooth the effects of the microscopic heterogeneities [7,8,17]. The right-hand side of Eq. (2) requires that variations in averaged quantities occur over a distance L that is large compared to the size r_m of the averaging volume [25,26].

When Eq. (2) is valid, the REV can be treated as a unit cell in a spatially periodic porous medium and a "closure problem" [24,27,28] can be developed (Eqs. (3)) at the microscopic scale, over the unit cell, whose numerical solution yields the permeability tensor $\underset{\approx}{K}$ (Eq. (4)) appearing in DARCY's law

$$\begin{aligned}
&-\underset{\sim}{\nabla} \underset{\sim}{d} + \nabla^2 \underset{\approx}{D} = \underset{\approx}{I}, \\
&\underset{\sim}{\nabla} \cdot \underset{\approx}{D} = \underset{\sim}{0}, \\
&\underset{\approx}{D} = \underset{\approx}{0} \quad \text{at } A_{\beta\sigma}, \\
&\text{Periodicity}: \quad \underset{\approx}{D}(\underset{\sim}{r}_{\beta} + \ell_i) = \underset{\approx}{D}(\underset{\sim}{r}_{\beta}), \ \underset{\sim}{d}(\underset{\sim}{r}_{\beta} + \ell_i) = \underset{\sim}{d}(\underset{\sim}{r}_{\beta}), \\
&\langle \underset{\sim}{d} \rangle^{\beta} = \underset{\sim}{0},
\end{aligned} \tag{3}$$

$$-\varepsilon \langle \underset{\approx}{D} \rangle^{\beta} = \underset{\approx}{K}. \tag{4}$$

The geometrical nature of the closure problem (Eqs. (3)) demonstrates theoretically that K is an implicit function of the micro-geometry included in the unit cell (Eq. (5)) [24,27,28]

$$\underset{\approx}{K} = \mathscr{f}(\text{micro-geometry}). \tag{5}$$

Eqs. (1)–(4) provide the most general framework for evaluating a property such as K as a function of microscopic features (Eq. (5)). Nonetheless, the filtered output K remains difficult to relate directly to the input geometry in the form of a 3D discrete image consisting commonly of about 10^9 solid or fluid *voxels* (volume elements) [30]. In order to advance our understanding of the relation between the micro-geometry and K it remains to express Eq. (5) into the more predictive framework outlined by Eqs. (6) and (7) [31,32]

$$\text{micro-geometry} = \mathscr{g}(P^i_{i=1,N}), \tag{6}$$

$$\underset{\approx}{K} = \mathscr{h}(\mathscr{p}^i_{i=1,\mathscr{N}}), \quad (\mathscr{p}^i_{i=1,\mathscr{N}}) \subseteq (P^i_{i=1,N}). \tag{7}$$

Relation (6) expresses that the micro-structure of the porous medium is completely characterized by a set of N geometrical parameters, noted $P^i_{i=1,N}$. K may be then expressed as an implicit function $\mathscr{h}$ of a sub-set of parameters, noted $\mathscr{p}^i_{i=1,\mathscr{N}}$, included in the complete set $P^i_{i=1,N}$ and describing the part of the micro-geometry relevant to K (Eq. (7)). In the predictive framework outlined by Eqs. (6) and (7), the essential difficulty lies in choosing the correct $\mathscr{p}^i_{i=1,\mathscr{N}}$. In our approach, the description of K by a set of $\mathscr{p}^i_{i=1,\mathscr{N}}$. will be declared appropriate if synthetic numerical porous media possessing similar transport properties than the real medium can be generated from the $\mathscr{p}^i_{i=1,\mathscr{N}}$. The objective of the current work is to ensure the ability of a class of random models for porous micro-structures to portray all the critical properties of real, observed, porous media.

2. Introduction

A porous material may always be interpreted as produced by a general process varying as a function of time t and spatial coordinates. In the case of cement and concrete composites, this process may involve hydration processes and degradation processes due to environmental aggressive agents (e.g. CO_2, chloride ions). For geological porous media, this process would rather include depositional processes (e.g., hydrodynamics, bioturbation), early post-depositional processes and post-lithification processes (e.g., pressure solution, tectonic deformation).

Whatever the class of porous media, the porous medium exists in a well defined region of space, noted $\mathscr{V}(r)$, whose boundaries $\partial\mathscr{V}(r)$ are fixed by the length-scales and time-scales of the involved causal processes.

In the context of the random model considered herein, synthetic numerical porous media are produced as realizations of a random stationary ergodic function [12] characterized by its probability density function (PDF) and autocorrelation function (ACF) measured on a finite sample $\upsilon(r)$ of the studied porous medium. The size υ and the boundaries $\partial\upsilon(\underset{\sim}{r})$ of the sampling

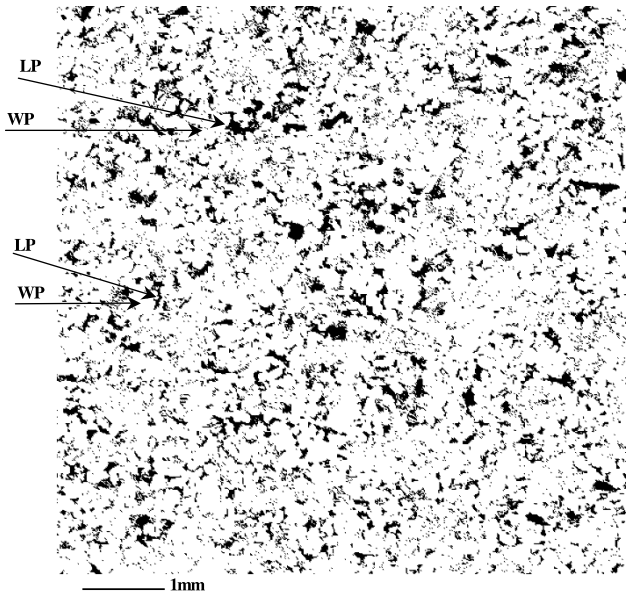

Fig. 1. 512×512 binary (0–1) digital image from an Upper Shoreface Sandstone. Image Size: 6.9×6.9 mm; pixel edge: $T = 13.57$ μm. Porosity expressed by black and solid phase by white. The porosity, ε, is 0.15. *WP*: well-packed grain local aggregate. *LP*: loose-packed pore, or packing flaw.

window are, as always, dictated by either practical, logistic or economic considerations: in particular we have: $v \ll \mathscr{V}$ [33]. As far as we are concerned, the available sample, $v(\underset{\sim}{r})$, will be essentially a 2-D thin section of a few cm^2 (Fig. 1).

The random model is based on previous work in the fields of communications, electrical network analysis and defense systems, where a variety of algorithms have been developed for simulating random 1-D signals through a probabilistic approach [34–38]. Borrowing from these works, others generalized the theory to 2-D and 3-D porous media, mainly Joshi [39] and Quiblier [40], respectively. In this now quite popular approach [41–47], the random model is meant to portray the results of the causal processes at the origin of the real observed porous medium, i.e., all the essential geometrical features of the observed porous medium as they are expressed in the finite sample $v(\underset{\sim}{r})$. The objective of our contribution is to ascertain whether or not this is true.

3. Theoretical background

The porous medium is described by a set of random variables characterized by a probability density function PDF and an autocorrelation function ACF. The model is a straightforward generalization [39,40] of a 1-D model [34–38]. The model produces a series of $n - D_{n \geqslant 2}$ sets of random numbers having any desired PDF and ACF. The algorithm relies on suitable linear and non-linear filters to transform a $n - D$ set of Gaussian random numbers into a binary set with the desired PDF and ACF. The only geometrical information which is imposed in the model is contained in the two functions fitted in the process, the PDF and the ACF.

The current work is related to 2-D outputs generated from 2-D ACFs and PDFs measured on finite digital binary images of type Fig. 1 as a necessary step towards the *controlled* generation of 3-D outputs from measurements performed on 2-D conventional petrographic thin sections.

Fig. 1 comprises 512×512 *pixels* (picture element; pixel size $T = 13.57$ μm) portraying pixels of one class (in our case porosity) by one single intensity (1) and the remainder (the rock matrix) by another (0). Fig. 1 is a sub-sample of a 2048×2048 digital image from an Upper Shoreface Sandstone (North Sea) consisting of 4×4 non-overlapping elementary views (each 512×512 pixels) acquired on a Scanning Electron Microscope in back-scattered mode [48], binarized and then merged into a high resolution mosaic of size about 3×3 cm^2.

An example of output from the random model is shown in Fig. 2.

A binary image of type Fig. 1 may be described by the discrete phase function $\varkappa$ expressed by Eq. (8)

$$\varkappa(x,y) = \sum_{k=0}^{N-1} \sum_{l=0}^{N-1} \varkappa_{kT,lT} \delta(x - kT, y - lT), \tag{8}$$

where T ($T = 13.57$ μm) is the sampling interval in the local Cartesian directions, δ is the Dirac distribution

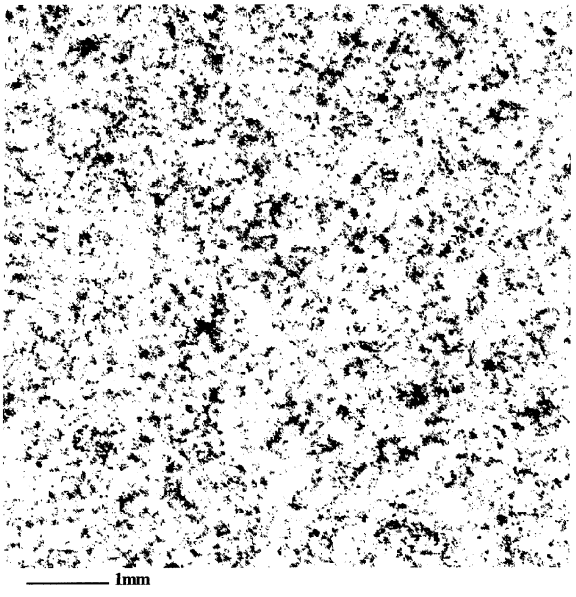

Fig. 2. 512×512 portion of a "quasi-infinite" synthetic digital image produced from the porosity ε and the ACF (Fig. 3) measured on the Upper Shoreface Sandstone of which a sample is displayed in Fig. 1. This realization should be viewed as a 2-D correlated noise [39]. Porosity is expressed by black. The porosity is 0.15.

[49]. The discrete phase function $\varkappa(x,y)$ comprises $N\times N$ samples. $\varkappa(x,y)$ is identically null out of its finite support of size $NT\times NT$. The PDF, when evaluated on a binary (0–1) image contains no more information than the porosity ε. In this respect, we will talk from now on about porosity rather than about PDF.

The porosity ε is expressed by

$$\varepsilon=\frac{1}{N^2}\sum_{k=0}^{N-1}\sum_{l=0}^{N-1}\varkappa_{kT,lT}. \tag{9}$$

The discrete 2-D ACF is defined by Eq. (10) [50]

$$\sigma_Z(rT,sT)=\sum_{k=0}^{N-1}\sum_{l=0}^{N-1}\dot{\varkappa}_{kT,lT}\dot{\varkappa}_{kT+rT,lT+sT}, \tag{10}$$

where $\dot{\varkappa}(x,y)$ represent the centered phase function $\dot{\varkappa}(x,y)=\varkappa(x,y)-\varepsilon$. In Eq. (10) $r,s=0,\pm1,\ \pm2,\ldots,\pm(N-1)$ and it is recalled that $\dot{\varkappa}(x,y)$ is identically null out of a finite $NT\times NT$ support.

The ACF is often interpreted as characterizing the dependence of a point $(kT+rT,lT+sT)$ upon a point (kT,lT) as well as the dispersion of the phase function $\varkappa$ about its mean (ε). The ACF is usually normalized by the variance, $\sigma_Z(0,0)$ so as not to include the dispersion effect. The normalized ACF $\rho_Z(r,s)(\rho_Z(r,s)=\sigma_Z(r,s)\sigma_Z^{-1}(0,0))$ provides information about the probability for a point $(k+r,l+s)$ and a point (k,l) to belong to the void phase [40]. And it is understood that k,l and r,s stand for kT, lT and rT, sT (this convention will be kept henceforth unless specified otherwise).

The simulation is three-fold:

1. A set of independent normally distributed random numbers x_{ij} is generated over a $M\times M$ 2-D grid.

2. The random variable X_{ij} is then passed through a linear filter defined by a $(\nu+1\times\nu+1)$ 2-D array of weighting functions (filter gains) a_{uv}. The random variable Y_{ij} at the output of the linear filter is related to the input X_{ij} by Eq. (11). As discussed further on, the size $(\nu+1\times\nu+1)$ of the 2-D array a_{uv} is related to the number of pixels ν at which the ACF is declared negligible, the so-called correlation length [51]. We will see in Section 4.1, that the evaluation made here for ν, is still wanting in that it carries with it some arbitrariness

$$y_{ij}=\sum_{u\in[0,\nu[}\sum_{v\in[0,\nu[}a_{uv}x_{i+u\,j+v}. \tag{11}$$

The weighting functions a_{uv} are scaled according to Eq. (12). The output of the linear filter Y_{ij} follows then a normal probability density function $\not{n}_Y(y_{ij})$ given by Eq. (13), and is correlated according to the ACF given by Eq. (14)

$$\sum_{u\in[0,\nu[}\sum_{v\in[0,\nu[}a_{uv}^2=1, \tag{12}$$

$$\not{n}_Y(y_{ij})=\frac{1}{\sqrt{2\pi}}\mathrm{e}^{-y_{ij}^2/2}, \tag{13}$$

$$\rho_Y(r,s)=\sum_{u\in[0,\nu[}\sum_{v\in[0,\nu[}a_{uv}a_{u+r,v+s}. \tag{14}$$

As justified further, the weighting functions a_{uv} in Eq. (11) are determined beforehand so as to yield the desired ACF $\rho_Y(r,s)$ at the output random set Y_{ij}. Similarly, the ACF $\rho_Y(r,s)$ at the output of the linear filter is also determined beforehand in a way that it will yield the specified $\rho_Z(r,s)$ at the binary output of the stochastic process Z_{ij}.

3. The linear output Y_{ij} (Eq. (11)) takes continuous values in $\mathbb{R}$ according to the PDF $\not{n}_Y(y_{ij})$ given by Eq. (13). But we want a binary random set at the output of the process Z_{ij}. To do so, a new variable, uniformly distributed between 0 and 1 and defined as the cumulative probability distribution $P_Y(y_{ij})$ of Y_{ij}, is associated to each random number y_{ij} (Eq. (15)). The intermediate variable $P_Y(y_{ij})$ is then subjected to the nonlinear filter given by Eq. (16) to impose the desired porosity at the binary output Z_{ij} [39–41].

$$y_{ij}\to P_Y(y_{ij})=\int_{-\infty}^{y_{ij}}\not{n}_Y(y)\,\mathrm{d}y=\frac{1}{\sqrt{2\pi}}\int_{-\infty}^{y_{ij}}\mathrm{e}^{-y^2/2}\,\mathrm{d}y, \tag{15}$$

$$z_{ij}=1\begin{cases}\text{if} & P_Y(y_{ij})\leqslant\varepsilon,\\ 0 & \text{otherwise.}\end{cases} \tag{16}$$

As mentioned above, the suitable ACF $\rho_Y(r,s)$ that will yield the specified ACF $\rho_Z(r,s)$ at the output of the nonlinear filter Z_{ij} (Eq. (16)) must be first determined prior to simulation. This is done capitalizing on valuable work by Barret and Coales [34], and Barret and Lampard [35] who showed that the ACF $\rho_Z(r,s)$ at the output of the nonlinear filter can be defined as a series of the normalized ACF $\rho_Y(r,s)$ at the input of the nonlinear filter as expressed by Eqs. (17) and (18)

$$\rho_Z(r,s)=\sum_{m=0}^{\infty}C_m^2\rho_Y(r,s)^m, \tag{17}$$

$$C_m=\frac{1}{\sqrt{2\pi m!}}\int_{-\infty}^{+\infty}\mathrm{e}^{-y^2/2}H_m(y)f(y)\,\mathrm{d}y. \tag{18}$$

In Eq. (18), $H_m(y)$ is the Hermite polynomial of order m [39] and $f(y)$ is a nonlinear characteristic given by Eq. (19) [41]:

$$\begin{aligned}f(y_{ij})&=\frac{\varepsilon-1}{\sqrt{\varepsilon(1-\varepsilon)}}\quad\text{if }\ P_Y(y_{ij})\leqslant\varepsilon,\\ f(y_{ij})&=\frac{\varepsilon}{\sqrt{\varepsilon(1-\varepsilon)}}\quad\text{if }\ P_Y(y_{ij})>\varepsilon.\end{aligned} \tag{19}$$

Eqs. (17)–(19) allow, from measured ε and $\rho_Z(r,s)$, to determine by a NEWTON's method the suitable ACF

$\rho_Y(r,s)$ that will yield the desired ACF $\rho_Z(r,s)$ at the output Z_{ij}. With knowledge of $\rho_Y(r,s)$, relation (14) is then expressed as a system of nonlinear algebraic equations whose solution yields the correct $\aleph+1\times\aleph+1$ weighting functions a_{uv} of the linear filter that will yield the desired ACF $\rho_Y(r,s)$ at the output Y_{ij} of the linear filter (Eq. (11)).

The correlation length $\aleph$ is a length beyond which the measured ACF $\rho_Z(r,s)$ constraining the random process vanishes to zero (yielding in the obvious manner Eq. (20)) implying that the studied porous medium is homogeneous (stationary ergodic in the statistical lingo [51])

$$a_{uv}=0 \quad \forall u \text{ and/or } v>\aleph. \tag{20}$$

The search for the a_{uv} solution of the nonlinear system (Eq. (14)) is performed using the robust Vignes' method [52] at a high computer time cost. As usual, the smaller the correlation length $\aleph$, the lower the computer time needed.

In the considered 2-D anisotropic case, the nonlinear system (Eq. (14)) is over-determined. So that the solution a_{uv} are obtained in a least squared sense, i.e., approximately. The implication of this is that the desired ACF $\rho_Z(r,s)$ at the output Z_{ij} of the process can only be imposed approximately. This is a big difference (not reported elsewhere to the author's knowledge) with the 1-D case or isotropic case where the number of unknowns is equal to the number of equations. The consequences of this difference between the 1-D case and the $n-D_{n\geqslant 2}$ case will be discussed in Section 4.2.

Knowledge of the suitable a_{uv} and $\rho_Y(r,s)$ permits to generate, through steps 1–3, a set of $\mathscr{M}$ binary (0–1) random fields $Z_{ij}^{k,k=1,\mathscr{M}}$ with specified ε and approximate ACF. Fig. 2 provides an example of a numerical realization of the random process.

The linear and nonlinear operators expressed by Eq. (11), (15) and (16)), respectively are applied directly on a point by point basis to the input Gaussian $M\times M$ random variable X_{ij}. The size $M\times M$ of the binary (0–1) output of the simulation Z_{ij} is accordingly not limited (and can be much larger than the imposed correlation length $\aleph$). In this respect, the numerical realizations of the random process are termed "quasi-infinite" porous media. And by quasi-infinite it is meant that every synthetic realization of size $M\times M$ may be formed by the replication of a quasi-infinite number of elementary volume of size $\aleph\times\aleph$ ($\aleph\ll M$), each containing the geometrical information carried by ε and the ACF fitted in the model. Because the process does not impose to the initial uncorrelated Gaussian $M\times M$ input set X_{ij} any correlation beyond a square window $|\aleph|$, $|\aleph|$, every realization $Z_{ij}^{k,k=1,\mathscr{M}}$ is expected to be uncorrelated at scales larger than the imposed correlation length.

4. Hypothesis of the random model for porous micro-structure

Our objective is to ascertain the ability of the current random generator to produce synthetic media carrying all the critical geometrical features of real, observed, porous material (for example Fig. 1). A positive answer requires two conditions [40]:

1. the sampled porous medium is homogeneous,
2. the two parameters $P_{i=1,2}^{i}=(\varepsilon,\text{ACF})$ constraining the generator carry all the essential information about the micro-structure.

4.1. Homogeneity of the porous medium

The porous micro-structure being treated as a realization of a stationary ergodic random process, it must be homogeneous. The achievement of stationarity-ergodicity (homogeneity) is commonly based on physical considerations about the nature of the process of interest [51]. Quoting from Quiblier [40] "...stationarity would appear to be borne out by observation...". This is to say that, from our standpoint, homogeneity is commonly assumed rather than quantified.

In the current random generator, stationarity-ergodicity is associated to a property of the measured ACF: the existence of a distance, the correlation length noted $(|\aleph|,|\aleph|)$ (that may be direction-dependent), from which onwards the ACF tends towards zero (Eq. (21)). Eq. (21) is the criterion explicitly accounted for to develop a nonlinear system (Eq. (14)) computationally tractable, where a *finite number of unknowns* are to be evaluated (Eq. (20))

$$\rho_Z(r,s)\cong 0 \quad \text{for } |s|>|\aleph| \text{ and/or } |r|>|\aleph|. \tag{21}$$

Eq. (21) means that two points r,s spaced apart such that $|r|>|\aleph|$ and/or $|s|>|\aleph|$ are uncorrelated. That is to say, at scales larger than $(|\aleph|,|\aleph|)$ the micro-geometry is unstructured (homogeneous) [50]. The correlation length $(|\aleph|,|\aleph|)$ is analogous to the characteristic length r_m associated to the geometrical REV as introduced by Eq. (2). An ACF measured on a digital image of type Fig. 1, exhibits "universal" characteristics: a central peak at small lags r, s (of maximum value equal to 1 at lag 0, 0) decreasing rapidly, and then a 2-D train of small fluctuations or peaks around 0. Generally, it is assumed that when the fluctuations get too small – here small is arbitrary – they are no longer significant and can be zeroed in accordance with Eq. (21). As others [40,41], we follow that route and zero the measured ACF beyond an arbitrary length chosen here roughly equal to |0.5| mm along both Cartesian directions. Fig. 3 shows the sub-part $\hat{\rho}_Z(r,s)$ of the

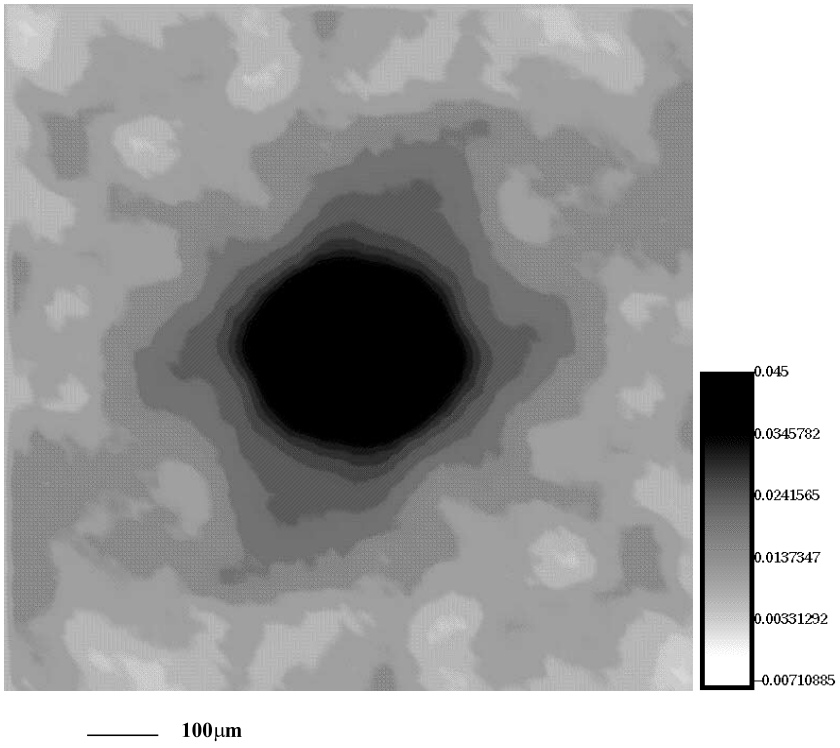

Fig. 3. 2-D anisotropic subpart of the ACF $\rho_Z(r,s)$ measured on the Upper Shoreface Sandstone in Fig. 1, noted $\hat{\rho}_Z(r,s)$ and used as constraint in the random process. Horizontal lags s (resp. vertical, r) range from left to right (resp. top to bottom) from -31 to $+31$. Lag $0,0$ is located at the center of the display ($\hat{\rho}_Z(0,0)=1$). Lags are calibrated in units of length (pixel edge $T=13.6$ μm) (r,s stand for rT, sT). The correlation length assumed for the simulation ($\mathscr{n}=\pm 31$) is roughly ± 0.5 mm along both Cartesian directions. So as to see the small peaks of $\hat{\rho}_Z(r,s)$, the central peak was truncated. All the central values of $\hat{\rho}_Z(r,s) \geqslant 0.045$ and $\leqslant 1$ are represented by the same black color (see gray level map legend). This figure highlights a universal characteristic of ACF functions: a big peak at small lags, of maximum value equal to 1 at lag $0,0$ which then decreases rapidly towards 0. By means of the discrete correlation theorem, the ACF is calculated in the Fourier domain capitalizing on fast Fourier transform algorithms.

ACF measured on Fig. 1, and fitted in the random model.

The arbitrariness of the choice for the correlation length ($|\mathscr{n}|$, $|\mathscr{n}|$) is still wanting. We will keep in mind that the zeroed fluctuations of the measured ACF may carry a relevant geometrical information to be eventually fitted in the random model. The (further) examination of the simulated micro-structures may confirm or infirm at least qualitatively the latter point. Because the scale of homogeneity is here rather assumed than quantified, further work should concern the development of more objective criteria to identify the correlation length. Along that line, we report the criterion proposed among others by Quintard and Whitaker [22]: a porous medium is homogeneous with respect to a volume V if

$$\nabla \langle \underset{\sim}{y} \rangle^{\beta} \ll 1, \tag{22}$$

where $\langle\rangle^{\beta}$ denotes the intrinsic volume average operator taken over V; $\underset{\sim}{y}$ is a position vector within the fluid (β) phase, relative to the centroid of the volume V.

4.2. Quantity and nature of the information carried by a measured ACF

Answering to whether or not the porosity and the ACF carry all the critical information about the microstructure is a major challenge. Of course a qualitative answer may be provided by examining the simulated micro-structures (Fig. 2 for example) [40]. From a visual point of view, the synthetic medium in Fig. 2 looks similar to the real Upper Shoreface Sandstone. And this visual resemblance suggests qualitatively that the ACF (and ε) measured on a finite sample $\upsilon(r)$ synthesize the essential characteristics of a homogeneous porous medium $\mathscr{V}(r)$. We take advantage of the current contribution to provide a much more quantitative argumentation relating to the nature and quantity of information carried by a measured ACF. And to do so, we rely on work in such fields as astronomical speckle imaging, imaging correlography [53], spectroscopy where one is commonly faced with the problem of inferring an object's digital image $\varkappa_{k,l}$ of finite size ($\varkappa_{k,l}$ is non-zero only within a finite region of space) from

knowledge of its measured (and non-centered) ACF $\sigma_{r,s}$ [54,55] (Eq. (10)). Retrieving an image $z_{k,l}$ from its ACF being commonly encountered in the context of general imaging, a variety of *practical solutions* have been accordingly developed [54,56–66]. The most efficient solution is undoubtedly Fienup's [57] iterative Fourier transform (IFT) algorithm.

Fienup's algorithm allows to recover to within a pixel, in a heuristic manner, a digital image $z_{k,l}$ from:

- its measured ACF $\sigma_{r,s}$ and,
- some support constraint: the knowledge of the smallest closed set outside which $z_{k,l}$ is zero. As far as we are concerned, this support constraint is applied in a very loose-sense using a squared $N \times N$ estimate support whose "edge" N is straightforwardly computed as half the edge of the ACF support [67] (in accordance the sampling theorem [68,69])

Appendix A provides a short summary of Fienup's IFT loop. In all our computer experiments, starting from different initial guess, Fienup's IFT algorithm yields systematically to the binary digital image $z_{k,l}$ associated to the measured $\sigma_{r,s}$, suggesting that there are no multiple solutions to recovering a binary digital image from its ACF. Extension to the 3-D case is straightforward. However, the 1-D case is very different and contains inherent multiple solutions [61].

The IFT procedure is illustrated hereafter by a computer experiment yielding the binary image of a Tidal Channel Sandstone (Fig. 4) from its associated ACF (Fig. 5). The initial guess $g_0(x,y)$ for the 256×256 image to be inferred (Fig. 4) is a realization of a normally distributed random field. Figs. 6–10 represent the estimates $g_{12}(x,y)$, $g_{2100}(x,y)$, $g_{2580}(x,y)$, $g_{3700}(x,y)$ and $g_{6520}(x,y)$ of the image to be inferred (Fig. 4) after 12, 2100, 2580, 3700 and 6520 iterations, respectively. In Fig. 7, some geometrical features of the sought image are already distinguishable in the estimate $g_{2100}(x,y)$. In Figs. 8 and 9, most of the geometrical features are recovered and in Fig. 10, the estimate $g_{6520}(x,y)$ is exactly the sought binary image, to within a pixel. The use of different random initial guess yielded systematically to the digital image displayed in Fig. 4. The readers may refer to Anguy et al. [32] for a more complete report of that type of computer experiments applied to images of porous materials.

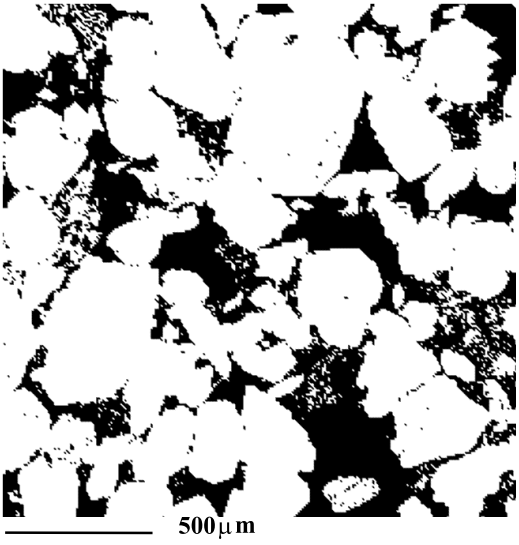

Fig. 4. 256×256 binary (0–1) digital image from a Tidal Channel Sandstone (North Sea). Image size: 1.74×1.74 mm; pixel edge: $T = 6.79$ μm. Porosity expressed by black and solid phase by white. The porosity is 0.27.

The IFT algorithm shows heuristically that it exists a one to one, i.e., bijective, relation between a finite binary digital $n - D_{n \geqslant 2}$ object and its ACF. In other words, a measured ACF contains all the information about the geometrical features included in the finite support it is measured on. This fundamental property of a measured ACF implies that no random model can impose exactly a specified $n - D_{n \geqslant 2}$ ACF over a set of binary realizations. One may find some consistency between the latter implication and the remark made in Section 3 that, as soon as the specified $n - D$ ACF is of dimension $n \geqslant 2$, the studied random model cannot impose exactly the specified ACF at the binary (0–1) outputs (due to the over determined character of the system (Eq. (14)) yielding the a_{uv}).

It may be important to summarize, at this point, what has been done. We observe the micro-structure of a porous medium $\mathscr{V}(r)$ through an available finite sample $v(r)$ (thin section). Relying on the homogeneity assumption (Section 4.1), we interpret the available (unique) real sample $v(r)$ as a realization, among an infinite set considered as possible [73], of a random function characterized by its PDF and ACF. From that point view, the ACF is a probabilistic quantity. Because there is no general agreement on the ability of the ACF to portray the essential structural characteristics of a homogeneous porous medium $\mathscr{V}(r)$, we rely in Section 4.2 on Fienup's iterative loop [57] to ensure the richness of the information carried by the ACF. From the point of view developed in Section 4.2, the measured ACF is a deterministic parameter. One may "unify" these probabilistic and deterministic interpretations by considering that the measured ACF is made of two parts:

1. an information that synthesizes the essential (statistical) characteristics of the geometry of the porous medium $\mathscr{V}(r)$. It is the probabilistic component of the measured ACF [32,50,73],
2. an information about the influence of the finiteness of the boundaries $\partial v(r)$ of the sampled window $v(r)$. It is the deterministic component of the measured ACF. The deterministic part expresses that the finite

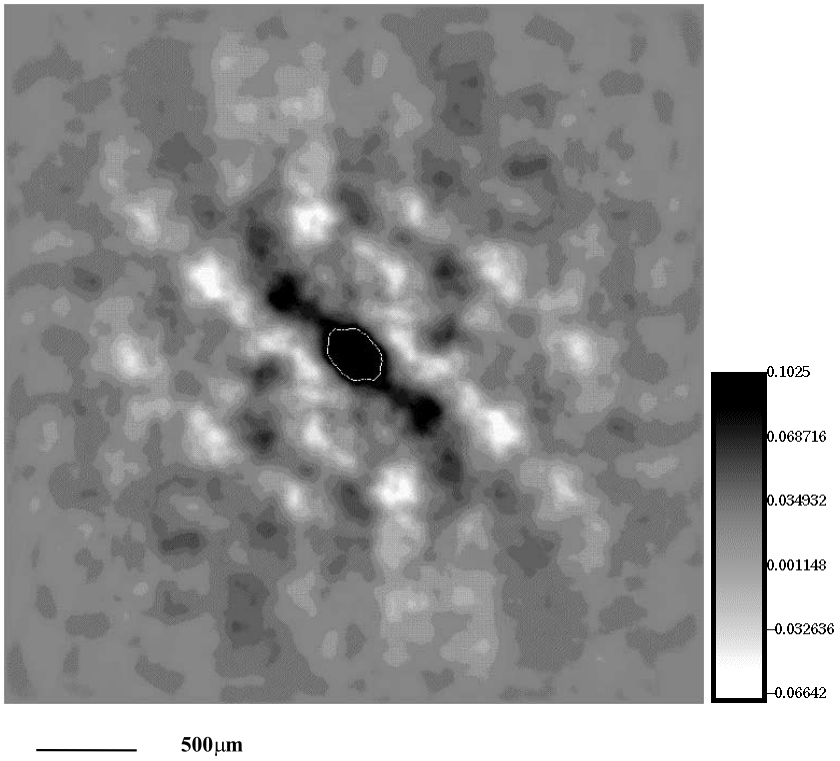

Fig. 5. 2-D (anisotropic) ACF $\sigma_{r,s}$ measured on the Tidal Channel Sandstone in Fig. 4. In this display the ACF is centered [51] and normalized by the variance $\sigma_{0,0}$. Lags r, s are calibrated in unit of length T (pixel size $T = 6.79$) and range from -255 to $+255$ (-1.73 mm to $+1.73$ mm) along both Cartesian directions. Lag $0, 0$ is at the center of the display. To see the small peaks of the ACF, all the values of the ACF $\geqslant 0.1025$ and $\leqslant 1$ (bounded by the white line around the central peak of the ACF) are represented by the same black color (see gray level map legend).

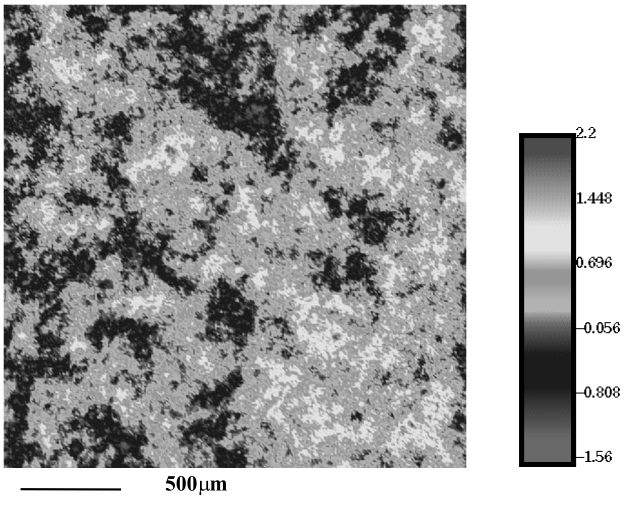

Fig. 6. Current 256×256 estimate $g_{12}(x, y)$ (after 12 iterations of the IFT algorithm [57]) of the image to be recovered (Fig. 4) from the only knowledge of its ACF (Fig. 5). The object space normalized root-mean-squared error metrics used to monitor the convergence of the algorithm is $E_{O,12} = 0.189$ where $E_{O,k}$, the error at the kth iteration is given by (see Appendix A for notations)

$$E_{O,k} = \left(\frac{\sum_{x,y \in \gamma} (g'_k(x,y))^2}{\sum_{x,y} (g'_k(x,y))^2} \right)^{1/2}.$$

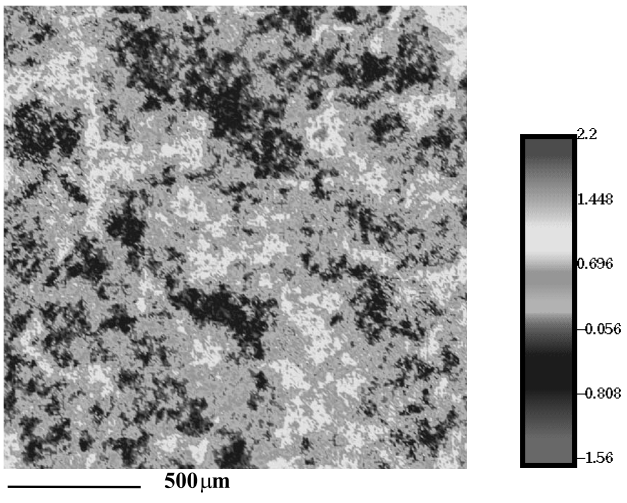

Fig. 7. Current estimate $g_{2100}(x, y)$ after 2100 iterations ($E_{O,2100} = 0.078$).

sample image is isolated in a unique manner in an "infinite fields of zeros" [50,73]; whence the unique reconstructions using Fienup's [57] IFT algorithm. The finite boundaries are not "impassable": the calculation of the ACF passes through the finite

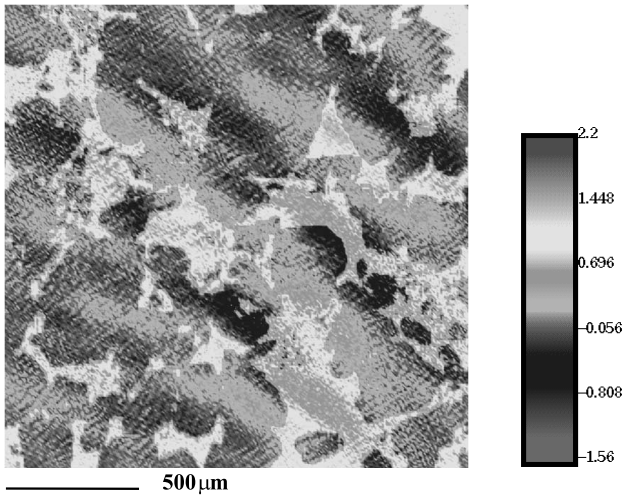

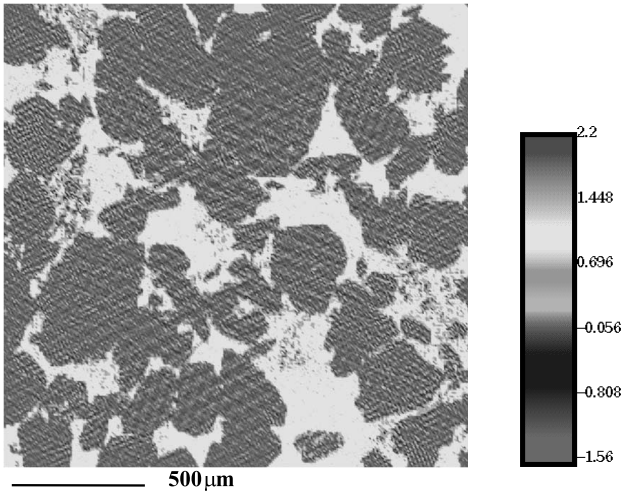

Fig. 9. Estimate $g_{3700}(x,y)$ after 3700 iterations ($E_{O,3700} = 0.021$).

frontiers $\partial\nu(r)$ (Eq. (10)) [50,73]. The deterministic part expresses ''edge-effects'' and is related only to finite sample $\nu(r)$ as confirmed by the IFT algorithm. It cannot be reproduced across a series of binary realizations of the random process.

We will conclude this paragraph by the following remark: it is to hope that the part of the measured ACF that is not reproduced by the random model due to the over-determined nature of the nonlinear system (Eq. (14)) is related to deterministic part of the ACF. At present, we have no rigorous criterion to validate this hypothesis. The next section is devoted to the analysis of the simulated micro-structures.

5. Simulated micro-structures

As illustrated for the Upper Shoreface Sandstone in Fig. 1, porosity on 2-D sections appears as many discrete patches of porosity often referred to as PORELs (PORe ELements) identified as closed areas of porosity. At the thin-section-scale, up to a few cm^2 (resp. at the plug-scale up to a few cm^3) the structural complexity arises from episodic fluctuations in the depositional dynamics, yielding a hierarchy of structural components ranging from individual grains and PORELs up to a single lamina as in Fig. 1 or a few lamina [31,74–78]. The fundamental structural component, the first level in a hierarchy, consists of oversized PORELs representing the site of loose packing, or flawed packing, embodied in a matrix of local aggregates of more efficiently packed grains (Fig. 1). The reasons for the universal occurrence of this domainal fabric (loose-packed domains versus well packed domains) were given in a seminal paper by Graton and Fraser [79] on the inevitable occurrence of zones of loose packing that are the consequence of the dynamic of the sedimentation process. In mechanically formed aggregates such as sandstones, formed by the simultaneous sedimentation of grains, many foci of close packing form simultaneously, but no process exists to produce the mutual parallel alignment of their internal fabric (i.e., a global closely packed condition) [74–79]. As the well-packed local aggregates grow towards another a compromise continuous zone of loose packing is formed. This domainal fabric has been verified and argumented over the years [31,74–78,80]. In ascending length scales, second-order structures consists of loose-packed zones that coalesce into continuous circuits throughout a matrix of close-packed domains [74–76,78]. Third-order structures concern various modes of clustering of the loose-packed circuits, as well as contrast between grain size producing for example lamina.

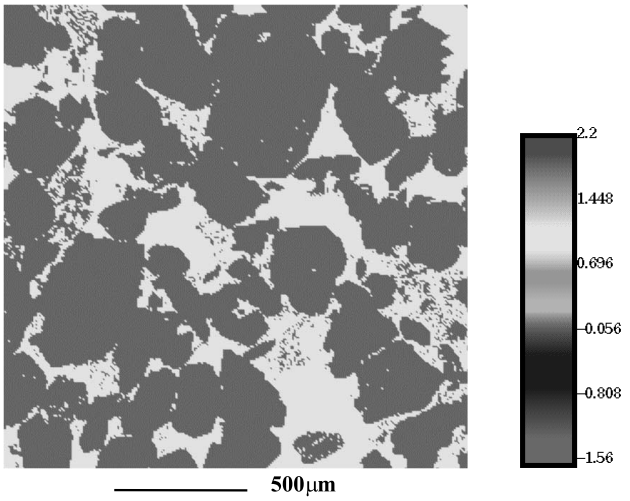

Fig. 10. Estimate $g_{6520}(x,y)$ after 6520 iterations. $E_{O,6520} = 9 \times 10^{-7}$, the algorithm has converged towards the searched image displayed in Fig. 4.

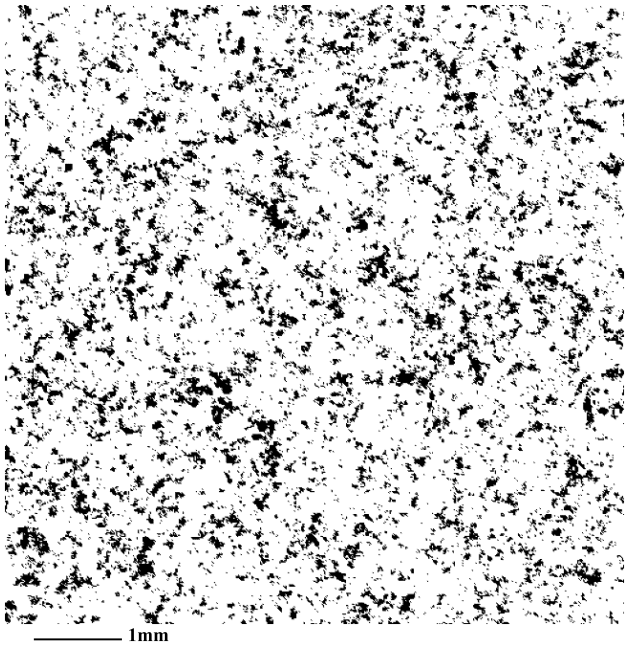

Fig. 11. 512×512 portion of a second "quasi-infinite" synthetic digital image produced from the porosity ε and the ACF (Fig. 3) measured on the Upper Shoreface Sandstone displayed in Fig. 1. The porosity of the simulated medium is 0.15.

Figs. 2 and 11 are examples of synthetic 2-D media generated from porosity and ACF (Fig. 3) measured on the real Upper Shoreface Sandstone in Fig. 1. The truncated ACF $\hat{\rho}_Z(r,s)$ fitted in the model has a correlation-length of ± 0.5 mm along both O_x and O_y. That is to say, information about the actual sample fitted in the random generator relates only to structural components of length $\leqslant 0.5$ mm. Beyond 0.5 mm, the synthetic media are expected to be uncorrelated. The porosity ε of the synthetic media in Figs. 2 and 11 is exactly 0.15 as for the real sample. The two synthetic media appear much similar to the actual. So that the media may be considered as belonging to the same class of porous media. From a visual standpoint, the size and shape of the individual PORELs are well reproduced in the synthetic realizations. In a previous contribution by Anguy et al. [31], such agreement between actual and simulated PORELs was quantified in the case of a series of Pennsylvanian Subsurface sand units samples by subjecting the real sand units sections and the synthetic sections to the same quantitative image analysis procedures [75]. As the real Upper Shore Face Sandstone (Fig. 1), the synthetic samples (Figs. 2 and 11) exhibit the fundamental domainal structure of all sandstones: juxtaposed domains of close-packed grains and loose-packed grains. This agreement was expected because, for the Upper Shore Face Sandstone in Fig. 1, the characteristic length of close-packed domains is of the order of the imposed correlation length.

Figs. 12 and 13 show the ACFs calculated on the numerical realizations in Figs. 2 and 11, respectively. The ACFs are displayed for lags $|r|$, $|s|$ smaller or equal to the imposed correlation length. The ACFs of the simulated media show small differences with the input ACF (Fig. 3). Such differences are consistent with the remarks made above that:

1. The desired ACF can be imposed only approximately on a set of binary (0–1) realizations due to the approximate determination of the filter gains a_{uv} (Eq. (14)). In this respect, the resemblance of either PORELs and first-order textural structure in the actual and synthetic samples suggests that the loss of information associated to the approximate assessment of the a_{uv} does not concern essential features of the actual sample.
2. The unicity of the relation between a binary image and its ACF implies that the synthetic media's ACFs and the actual sample's ACF must differ at least in their deterministic component expressing edge-effects related only to their respective support.

Fig. 14 displays another real sandstone of Tidal Channel type. Fig. 15 shows the synthetic medium obtained from the truncated ACF (lags $|r|$, $|s|$ smaller or equal to 0.5 mm) measured on the real sample (Fig. 14). One will note again the visual agreement between the PORELs and first-order textural component of the actual (Fig. 14) and synthetic sample (Fig. 15), highlighting the ability of the model to simulate a variety of classes of porous media.

The surprising result of these simulations is that actual and synthetic samples look similar at scales larger than the fitted correlation length. Over length-scales larger than $(|\mathscr{n}|, |\mathscr{n}|)$, loose-packed pores coalesce into similarly sized and shaped paths in either the actual and synthetic samples, highlighting the trace of 2-D circuits of over-sized PORELs, the second-order textural level of sandstones [31,74–81]. At even larger scales, third-order structures represented by the various modes of clustering of the circuits of over-sized pores look much similar.

The existence, within the synthetic media, of structural components of lengths larger than $(|\mathscr{n}|, |\mathscr{n}|)$ is obviously in contrast with the expected randomness of the synthetic realizations beyond $(|\mathscr{n}|, |\mathscr{n}|)$. The occurrence of those unexpected features is confirmed on the 2-D Fourier Density Power Spectrum (DPS; noted $|\mathscr{F}(v_x, v_y)|^2$) of the synthetic realizations. In the case of a $N \times N$ digital image the discrete vertical and horizontal wave numbers v_y, v_x, inversely proportional to wavelengths, takes the discrete values: $v_y, v_x = n/2NT$, $m/2NT, n, m = -N, \quad -N+1, \ldots, -1, 0, 1, \ldots, +N-1$. The DPS is a measure of the contribution to the total variance from wave numbers v_y, v_x. It quantifies the dominant heterogeneities whose length-scale $(v_x^2 + v_y^2)^{-1/2}$ and orientation $\tan^{-1}(v_y/v_x)$ are calibrated

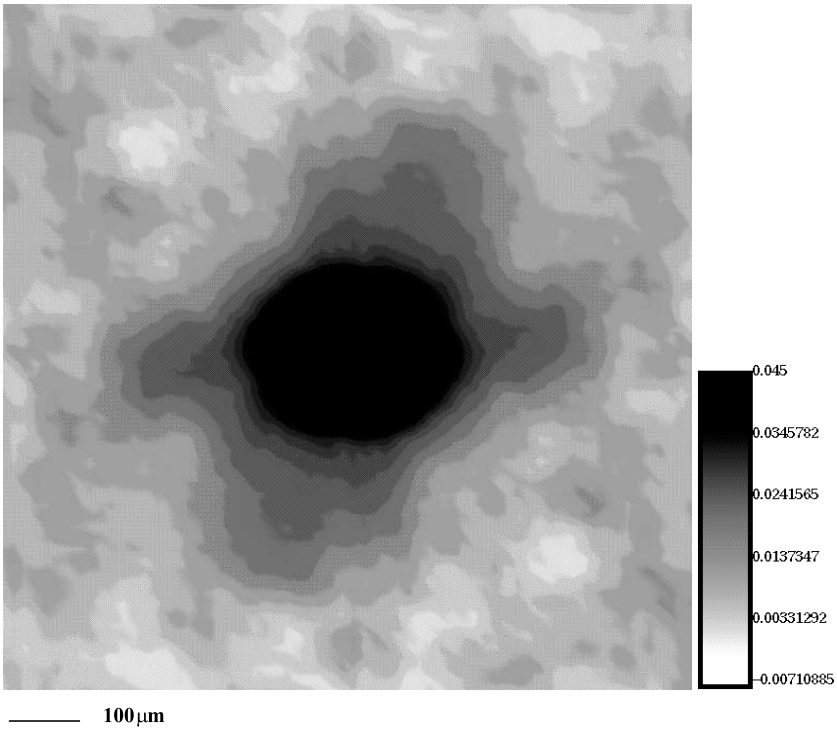

Fig. 12. Subpart ($|r|$ and $|s| \leqslant |\prime\prime|$) of the ACF of the simulated medium displayed in Fig. 2. Same conventions for the display as in Fig. 3. Note the small differences with between the current ACF and the ACF fitted in the random model (Fig. 3).

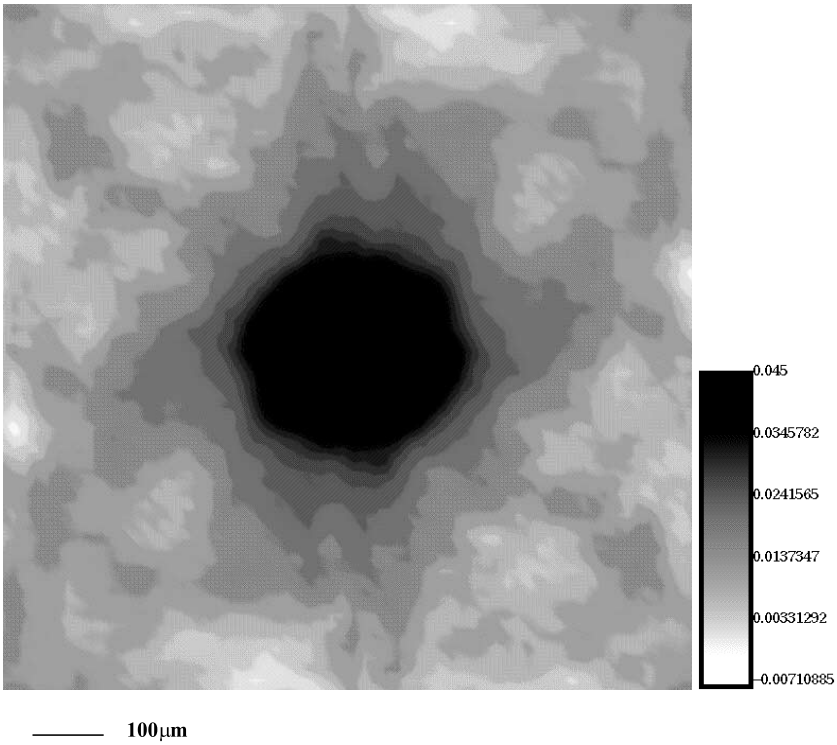

Fig. 13. Subpart ($|r|$ and $|s| \leqslant |\prime\prime|$) of the ACF of the simulated medium displayed in Fig. 11. Same conventions for the display as in Fig. 3.

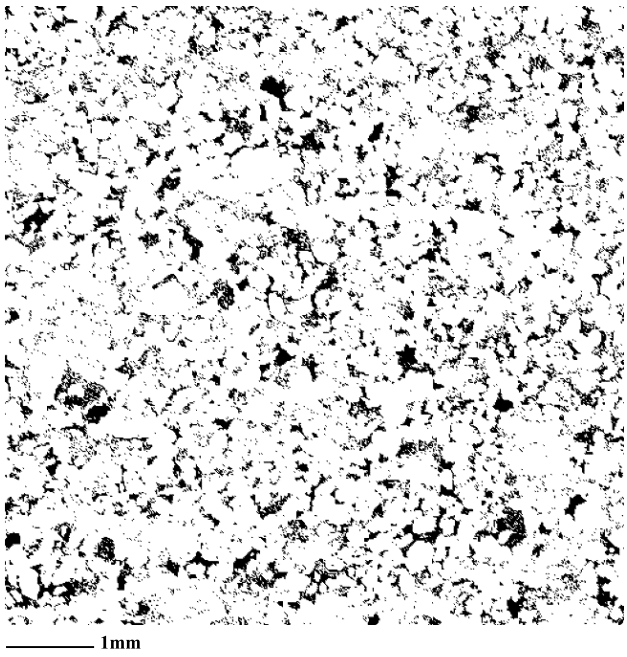

Fig. 14. 512×512 binary (0–1) digital image of a real Tidal Channel Sandstone (North Sea). Image Size: 6.9×6.9 mm; pixel size: $T = 13.57$ μm. Porosity expressed by black and solid phase by white.

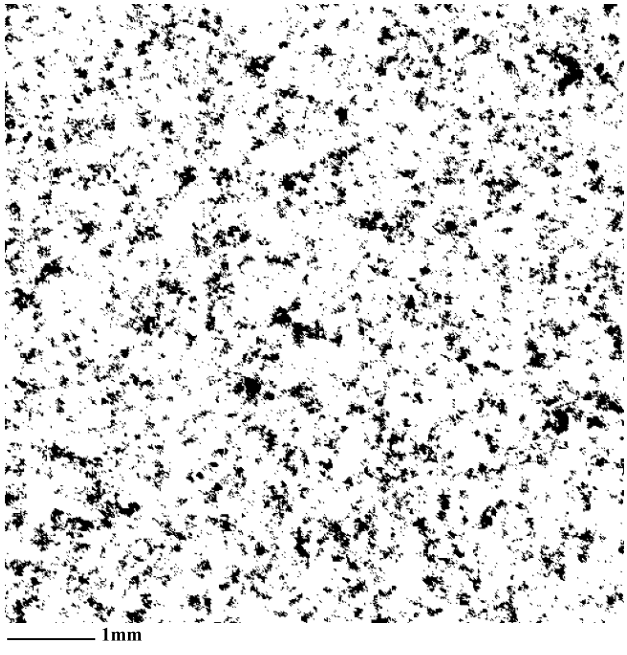

Fig. 15. 512×512 portion of a "quasi-infinite" synthetic digital image produced from the porosity ε and the truncated ACF (lags $|r|, |s|$ smaller or equal to 0.5 mm) measured on the Tidal Channel Sandstone displayed in Fig. 14.

by wave numbers [82]. The DPS (the squared of Eq. (A.1) is the Fourier Transform of the ACF [55,61,68,82–84]. In this respect, they characterize the same geometrical features. The advantage of using the DPS is that

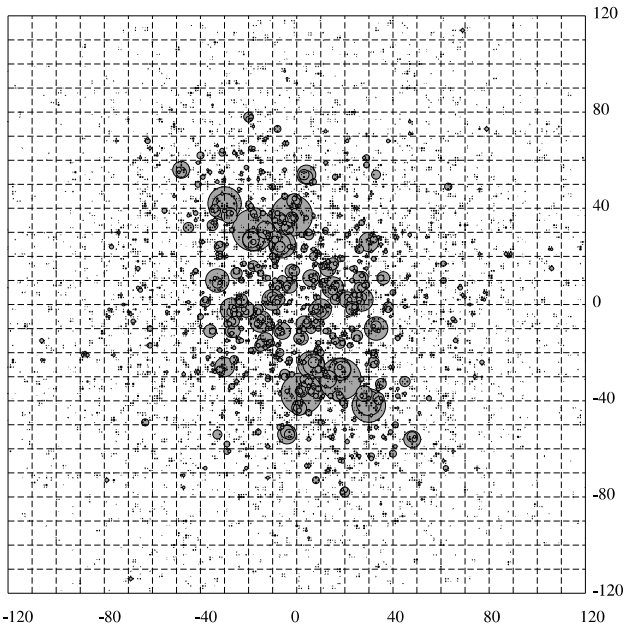

Fig. 16. 2-D Fourier power spectrum of a synthetic 1024×1024 realization of a Tidal Channel of which a 512×512 sub-sample is shown in Fig. 15. Numbers m, n on horizontal and vertical axes represent horizontal v_x and vertical v_y discrete wave numbers. Wave numbers v_x, v_y are proportional to the inverse of wave lengths λ_x, λ_y ($\lambda_y = 2NT/n, \lambda_x = 2NT/m$). The size of the circles is proportional to power. The largest the circle, the largest the relative contribution to the total variance from the underlying structural heterogeneity of scale and orientation calibrated by n, m. Power has been cubed to highlight the dominant scales of the heterogeneities (data representing location of low power are not plotted). High concentration of power at low wave numbers indicates the presence of a hierarchy of structural hetereogenities at scales much larger than the imposed correlation length of about 0.5 mm approximately associated to wave numbers |65|.

the information about large scale (low wave number) features is emphasized as illustrated by the DPS (Fig. 16) of the synthetic sandstone in Fig. 15. The DPS shows a high concentration of power at low wave numbers v_y, v_x expressing the existence of a hierarchy of large-scale heterogeneities. In Fig. 16, the dominant heterogeneity happens at wave numbers $v_y, v_x = +18, -31$ (resp. -18, $+31$) e.g., at a scale of about twice the fitted correlation length.

To understand the origin of these unexpected large scale in the synthetic realizations, we examined the mathematical properties of the ACF. As recalled in Appendix B, an ACF measured on a finite support is of zero spatial integral (0-energy).

The zeroing of the small peaks of the measured ACF $\rho_Z(r,s)$ beyond the assumed correlation length $(|\imath\imath|, |\imath\imath|)$ results in a truncated ACF $\hat{\rho}_Z(r,s)$ of non-0-energy, fitted in the random generator. On the other hand, the ACFs calculated on the synthetic realizations are of 0-energy (Appendix B) so that the 0-energy condition can only be restored through non-imposed peaks in the ACFs of the synthetic realizations occurring at lags

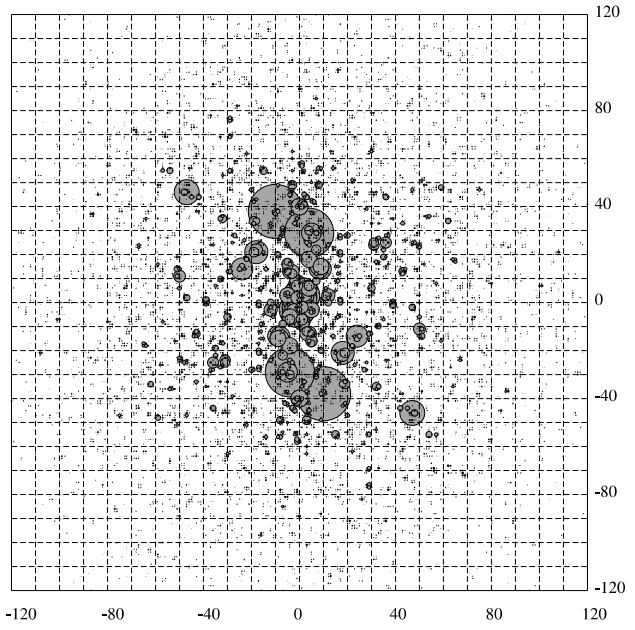

Fig. 17. 2-D Fourier power spectrum of a 1024×1024 digital binary image of a Tidal Channel Sandstone of which a 512×512 sample is shown in Fig. 14. Same conventions for the display as in Fig. 16.

$(|r|, |s|)$ larger than $(|\mathscr{n}|, |\mathscr{n}|)$. The length-scales and orientations of the additional structural features associated to these non-imposed peaks are determined by the values x_{ij} taken by the input random Gaussian population X_{ij} at the input of the model. Those additional non-imposed large scale heterogeneities within the synthetic realizations are in this respect random. They are associated with a structural noise produced by the non-rigorous use (from the theoretical point of view) of the random model: the truncated ACF $\hat{\rho}_Z(r,s)$ fitted in the random generator does not verify all the properties of an ACF. Nonetheless, from a more practical point of view, this unexpected structural noise participates to the satisfying visual aspect of the synthetic media. In this respect the actual samples must be also poorly structured, i.e., random, at large scales. The spatial distribution of the second- and third-order textural components in the actual media (Fig. 17) must also be poorly ordered, i.e., random. This is why, the synthetic media generated in this contribution can be considered as structural analogues of the actual poorly structured samples that we considered.

6. Conclusion and perspectives

In a transport context, that the achieved synthetic samples using the current random generator can be considered as analogues of their real counterparts is only "half a success". Indeed, as already delineated by Eqs. (6) and (7), our final objective is a comprehensive understanding of the relation between the micro-geometry and transport properties of porous media (such as K) in the context of the predictive framework recapitulated below by Eqs. (23)–(25)

$$P^i_{i=1,2} = (\varepsilon, \hat{\rho}_Z(r,s)), \tag{23}$$

$$\text{micro-geometry} = \mathscr{g}(P^i_{i=1,2}), \tag{24}$$

$$\underset{\approx}{K} = \mathscr{k}(\mathscr{p}^i_{i=1,\mathscr{N}}), \quad (\mathscr{p}^i_{i=1,\mathscr{N}}) \subseteq (P^i_{i=1,2}). \tag{25}$$

The 2-D structural analysis above reveals that the correct interpretation of relations (23)–(25) (using eventually 3-D synthetic realizations) requires the introduction of a third parameter P^3 noted ξ and accounting for the existence of a structural noise in the synthetic realizations to be used as inputs to the local volume averaging technique (Eqs. (3) and (4)). In the case of the simulated microstructures above, accounting for this third parameter would be particularly necessary since work by Ehrlich et al. [74,75] and McCreesh et al. [76] has demonstrated, using an empirical and independent approach, that structures of second-order (the circuits of loose-packing pores) are commonly responsible for more than 80% of the flow in natural aggregates such as sandstones. That is, relating to the achieved synthetic micro-structures, where second-order textural components are produced by an uncontrolled structural noise, parameter P^3 would yield the essential of the permeability.

A straightforward solution to decrease the impact upon flow of the non-imposed random structural features is to increase the correlation length fitted in the random model (and to verify at best the 0-energy condition) in order to *impose* second-order structures. This can be done of course only at a higher computational time cost. Yet, sansdtones being generally more structured that the Upper Shoreface and Tidal Channel examples presented herein, simulations involving larger correlation lengths are likely to be required in order to express faithfully the natural hierarchy of heterogeneities of real observed sandstones. So that simulations over larger correlation lengths need to be subjected to the petrograph expertise.

Also, it will be ultimately necessary to generate 3-D synthetic numerical porous media. A variety of natural mechanical aggregates such as sandstones are either statistically isotropic, or exhibit anisotropy in a single plane (perpendicular to the apparent bedding) [74–76]. One may capitalize on such observed properties to justify the use of 2-D conventional petrographic thin sections for *estimating* 3-D ACFs (that will produce the 3-D outputs) using the Hankel transforms [85,86]. One may also, as a first step, rely on 3-D input geometries obtained from modern techniques such as X-ray tomography combined with high intensity synchrotron sources [87].

It is important to emphasize that the results discussed above are consistent with the observations and theories concerning the arrangement of sedimented particles and the consequences of such arrangements on physical properties. The seminal work, albeit qualitative, of Graton and Fraser [79] has been verified and developed over the years. The emergence of digital imaging along with widely available computational resources has made possible quantification of the fabric. The generalization of that quantification using modeling involving first principles is the next short term step. As discussed above, in such models as the local volume averaging technique, permeability, for instance, is not imposed but emerges as a volume average of microscopic processes.

Extension of this approach to the field of cement, mortar and concrete should be a straightforward process, although the cement, mortar, and concrete systems are more complex, namely due to the presence of multiple components and of many scales of heterogeneities. The change in fabric and its effect on physical properties has been assessed in the geological framework as a function of temperature and pressure [88]. Thus there is promise that the evolution of artificial materials as they transform under the influence of thermodynamics can also be quantified.

The cement, mortar, concrete systems are different enough from most natural aggregates that the results of such an extension cannot be predicted in advance. In terms of particulates before reaction and solidification such aggregates tend to consist of extremely polymodal size frequency distributions with each mode contributed by a different constituent. If the fabric is homogeneous at small scales then the structural fabric could vary from that similar to an emulsion where particles of one sort "float" in a matrix of composed of the other sort to one where fine-grained particles occupy the interstices between larger particles. In either case the material need not be isotropic and attendant properties can be variable. However, is such an arrangement likely to occur, especially when the aggregate is mechanically mixed and vibrated? It is well known that such processes have a strong influence on the physical properties of the final product. This variation in properties with mechanical treatment must be a consequence of reorganizations of the fabric. Therefore even though the methodology and theory can be transferred to this new application, systematic investigations of these complex reactive mixtures will be necessary.

Acknowledgements

The authors would like to thank Marielle Bourget (GMMS, IUT de Reims, rue des Crayères, BP105, F-51687 Reims) for numerous and valuable discussions. The authors are very grateful to the reviewers who largely contributed to the improvement of this contribution.

Appendix A. The iterative Fourier transform (IFT) algorithm

The IFT algorithm due to Fienup [57] is an extension of the Gerchberg–Saxton algorithm [70,71]. The algorithm is an iterative loop bouncing back and forth between the Fourier-space where, the known Fourier modulus $|\mathscr{Z}_{vx,vy}|$ (Eq. (A.1)) of the image to be inferred $\varkappa_e(x,y)$ is applied and the object space where, a very loose square support constraint is enforced [54].

$$|\mathscr{F}(v_x,v_y)| = \left| \sum_{k=0}^{2N-1} \sum_{l=0}^{2N-1} \varkappa_{ekT,lT} e^{-2\pi j(v_x kT + v_y lT)} \right|. \tag{A.1}$$

As emphasized by Eq. (A.2), the Fourier constraint, i.e., the known Fourier modulus $|\mathscr{F}_{v_x,v_y}|$ of the sought image is computed directly from the measured ACF relying on the discrete correlation theorem [68,69]

$$\left|\mathscr{F}_{v_x,v_y}\right| = \sqrt{\mathrm{FT}(\mathrm{ACF})}, \tag{A.2}$$

where FT represents the direct Fourier transform [68].

The IFT algorithm has been already covered elsewhere. See for examples Fienup [57], Fienup and Wackerman [54] or Anguy et al. [32]. A very brief summary of its simplest version is provided below for sake of completeness. Each iteration within the IFT algorithm comprises the following four simple steps:

1. Fourier transform a current estimate $g_k(x,y)$ of the "zero-extended" image to be recovered $\varkappa_e(x,y)$. Subscript e (e for extended) recalls that the sought image is zero outside a $N \times N$ support.
2. Replace the Fourier modulus $|G_k(v_x,v_y)|$ of the computed Fourier transform by the known Fourier modulus $|\mathscr{F}(v_x,v_y)|$ to form an estimate of the Fourier transform.
3. Inverse Fourier transform the estimate of the Fourier transform to form $g'_k(x,y)$.
4. Make the minimum changes in $g'_k(x,y)$ to satisfy weak object domain constraints to form a new estimate $g_{k+1}(x,y)$ of the image to be inferred $\varkappa_e(x,y)$. The new input $g_{k+1}(x,y)$ is formed by zeroing $g'_k(x,y)$ if $g'_k(x,y)$ exceeds the known "diameter" of the image computed as half the diameter of the ACF. In practice, other forms of new input selections (that require no additional knowledge) are used in combination with the simple kind of input selection described above [32,54,57,62].

The convergence is monitored using normalized root-mean-squared error metrics in either Fourier- or object-

space [54] and the IFT algorithm continue till either of the squared error metrics is zero. Eq. (A.3) represent the object-space normalized root-mean-squared error

$$E^i_{O,k} = \left(\frac{\sum_{x,y\in\gamma} (g'_k(x,y))^2}{\sum_{x,y} (g'_k(x,y))^2} \right)^{1/2}. \quad \text{(A.3)}$$

In Eq. (A.3), γ denotes the set of points at which $g'_k(x,y)$ exceeds the diameter of the image, i.e., the points x,y such that x,y fall outside a squared $N \times N$ support representing an upper bound of the true object support [62,72].

Appendix B. Spatial integral of the ACF

Based on the discrete correlation theorem, the spatial integral of the ACF is given by Eq. (B.1) [50]

$$\sum_r \sum_s \sum_i \sum_j (\varkappa_{i,j} - \varepsilon)(\varkappa_{i+r,j+s} - \varepsilon) = |\mathscr{F}_{0,0}|^2, \quad \text{(B.1)}$$

where $\mathscr{F}_{0,0}$ is the value taken by discrete Fourier transform of the 0-appended function $\varkappa_{i,j} - \varepsilon$ at wave numbers $v_x, v_y = 0,0$.

As expressed by Eq. (B.2), it is obvious that $\mathscr{F}_{0,0}$ is zero

$$\mathscr{Z}_{0,0} = \sum_i \sum_j (\varkappa_{i,j} - \varepsilon) = 0. \quad \text{(B.2)}$$

One has immediately

$$\sum_r \sum_s \sigma_{r,s} = 0. \quad \text{(B.3)}$$

This demonstrates that the ACF has a spatial integral equal to 0, i.e., is of 0-energy.

References

[1] Bear J. Modeling flow and contaminant transport in fractured rocks. In: Bear J, Tsang C-F, de Marsily G, editors. Flow and contaminant transport in fractured rock. San Diego: Academic Press; 1993. p. 1–37.

[2] Bachmat Y, Bear J. Macroscopic modeling of transport phenomena in porous media 1: the continuum approach. Transp Porous Media 1986;1(3):213–40.

[3] Bachmat Y, Bear J. On the concept and size of a representative elementary volume (REV. In: Bear J, Corapcioglu Y, editors. Advances in transport phenomena in porous media. Dordrecht: Martinus Nijhoff; 1987. p. 3–20.

[4] Bear J, Braester C, Menier PC. Effective and relative permeabilities of anisotropic porous Media. Transp Porous Media 1987;2:301–16.

[5] Prat M. On the boundary conditions at the macroscopic level. Transp Porous Media 1989;4:259–80.

[6] Prat M. Modeling of heat transfer by conduction in a transition region between a porous medium and an external fluid. Transp Porous Media 1990;5:71–95.

[7] Bear J, Bachmat Y. Transport phenomena in porous media – Basic equations. In: Bear J, Corapcioglu Y, editors. Advances in transport phenomena in porous media. Dordrecht: Martinus Nijhoff; 1984. p. 3–62.

[8] Bear J. Dynamics of fluids in porous media. New York: Elsevier; 1972.

[9] Cushman JH. An introduction to hierarchical porous media. In: Cushman JH, editor. Dynamics of fluids in hierarchical porous media. New York: Academic Press; 1990. p. 1–6.

[10] Wheatcraft SW, Sharp GA, Tyler SW. Fluid flow and solute transport in fractal heterogeneous porous media. In: Cushman JH, editor. Dynamics of fluids in hierarchical porous media. New York: Academic Press; 1990. p. 305–26.

[11] Thompson AH. Fractal in rock physics. Annu Rev Earth Planet Sci 1991;19:237–62.

[12] Matheron G. Eléments pour une théorie des milieux poreux. Paris: Masson; 1967.

[13] Sanchez-Palencia E. Non homogeneous media and vibration theory. Berlin: Springer; 1980.

[14] Brenner H. Dispersion resulting from flow through spatially periodic porous media. Trans R Soc Lond 1980;297:81–133.

[15] Rubinstein J, Torquato S. Flow in random porous media; mathematical formulation; variational principles and rigorous bounds 1989;206:25-46.

[16] Anderson TB, Jackson R. A fluid mechanical description of fluidized beds. Ind Eng Chem Fundam 1967;6:527–38.

[17] Marle CM. Ecoulements monophasiques en milieux poreux. Revue Institut Français du Pétrole 1967;22:1471–509.

[18] Slattery JC. Flow of viscoelastic fluids through porous media. AIChE 1967;13:1066–77.

[19] Whitaker S. Diffusion and dispersion in porous media. AIChE 1967;13:420–7.

[20] Whitaker S. Flow in porous media I: a theoretical derivation of Darcy's law. Transp Porous Media 1986;1:3–25.

[21] Quintard M, Whitaker S. Transport in ordered and disordered porous media: volume-averaged equations, closure problems, and comparison with experiment. Chem Eng Sci 1993;48(14):2537–64.

[22] Quintard M, Whitaker S. Transport in ordered and disordered porous media I: the cellular average and the use of weighting functions. Transp Porous Media 1994;14:163–77.

[23] Quintard M, Whitaker S. Transport in ordered and disordered porous media II: generalized volume averaging. Transp Porous Media 1994;14:179–206.

[24] Quintard M, Whitaker S. Transport in ordered and disordered porous media III: closure and comparison between theory and experiment. Transp Porous Media 1994;15:31–49.

[25] Carbonell RG, Whitaker S. Heat and Mass transfer in porous media. In: Bear J, Corapcioglu MY, editors. Fundamentals of transport phenomena in porous media. Dordrecht: Martinus Nijhoff; 1984. p. 121–98.

[26] Nozad I, Carbonell RG, Whitaker S. Heat conduction in multiphase systems 1: theory and experiment for two-phase systems. Chem Eng Sci 1985;40(5):843–55.

[27] Barrére J, Gipouloux O, Whitaker S. On the closure problem for Darcy's law. Transp Porous Media 1992;7:209–22.

[28] Goyeau B, Benihaddadene T, Gobin D, Quintard M. Numerical calculation of the permeability in a dendritic mushy zone. Metall Mater Trans B 1999;30:613–22.

[29] Gray WG. A derivation of the equations for multiphase transport. Chem Eng Sci 1975;30:229–33.

[30] Garboczi EJ. Permeability, diffusivity and microstructural parameters: a critical review. Cem Conc Res 1990;20:591–601.

[31] Anguy Y, Bernard D, Ehrlich R. Towards realistic flow modeling. Creation and evaluation of two-dimensional simulated porous media: an image analysis approach. Surv Geophys 1996;17:287–365.

[32] Anguy Y, Ehrlich R, Mercet C. Is it possible to characterize the geometry of a real porous medium by a direct measurement on a

finite section? 1. The phase-retrieval problem. Math Geol 2001 in press.
[33] Bryant SL, King PR, Mellor DW. Network model evaluation of permeability and spatial correlation in a real random sphere packing. Transp Porous Media 1993;11:53–70.
[34] Barret JF, Coales JF. An introduction to the analysis of non linear control systems with random inputs. Proc IEE (London) 1955;Mono. 154. M103:190–9.
[35] Barret JF, Lampard DG. An expansion for some second order probability distributions and its application to noise problem. IRE Trans Inform Theory 1955;IT-1:10–5.
[36] Gujar UG, Kavanagh RJ. Generation of random signals with specified probability density function and power density spectra. IEEE Trans Autom Control 1968;716–9.
[37] Holiday EM. Transformation of a set of pseudo-random numbers into a set representing any desired probability and correlation. Report No. RE-TR-69-25, Alabama, Advanced Sensors Laboratory, Research and Engineering Directorate, U.S. Army Missile Command, Redstone Arsenal, 1969.
[38] Broste NA. Digital generation of random sequences with specified autocorrelation and probability density functions. Report No. RE-TR-70-5, Alabama, Advanced Sensors Laboratory, Research and Engineering Directorate, U.S. Army Missile Command, Redstone Arsenal, 1970.
[39] Joshi MY. A class of stochastic models for porous media. PhD Thesis, University of Kansas, 1974.
[40] Quiblier JA. A new three-dimensional modeling technique for studying porous media. J Colloid Interface Sci 1984;98(1):84–101.
[41] Adler PM, Jacquin CG, Quiblier JA. Flow in simulated porous media. Int J Multiphase Flow 1990;16(4):691–712.
[42] Adler PM. Porous media. London: Butterworth, Heinemann; 1992.
[43] Yao J, Frykman P, Kalaydjian F, Thovert JF, Adler PM. High-order moments of the phase function for real and reconstructed porous media: a comparison. J Colloid Interface Sci 1993; 146:478.
[44] Sallès J, Thovert JF, Adler PM. Transport in reconstructed porous media. In: Rouquerol J, Rodriguez-Reinoso F, Sing KSW, Unger KK, editors. Studies in surface science and catalysis, vol. 87. Amsterdam: Elsevier; 1994. p. 211.
[45] Giona M, Adrover A. Closed-form solution for the reconstruction problem in porous media. AIChE J 1996;42(5):1407–15.
[46] Ionnadis MA, Kwiecien MJ, Chatzis I. Electrical conductivity and percolation aspects of statistically homogeneous porous media. Transp Porous Media 1997;29:61–83.
[47] Ionnadis MA, Lange E. Micro-geometry and topology of statistically homogeneous porous media. In: Burganos VN, Karatzas GP, Payatakes AC, Brebbia CA, Gray WG, Pinder GF, editors. Computational methods in water resources XII, vol. 1. Southampton, UK: Computational Mechanics; 1998. p. 223–30.
[48] Tricart JP, Brévart O, Baranger R, Martinez L. Analyse quantitative d'images électroniques et chimiques. Boussens (FR): Société Nationale Elf Aquitaine; 1991.
[49] Roddier F. Distributions et transformation de Fourier. Paris: McGraw-Hill; 1985.
[50] Matheron G. Les variables régionalisées et leur estimation. Une application de la théorie des fonctions aléatoires aux sciences de la nature. Paris: Masson et Cie; 1965.
[51] Ventzel H. Théorie des probabilités. Moscou: Mir Moscou; 1973.
[52] Vignes J, Alt R, Pichat M. Algorithmes numériques – analyse et mise en oeuvre 2: équations et systèmes non linéaires. Paris: Technip; 1980.
[53] Idell PS, Fienup JR, Goodman RS. Image synthesis from non-imaged laser-speckle patterns. Opt Lett 1987;12:858–60.
[54] Fienup JR, Wackerman CC. Phase retrieval stagnation problems and solutions. J Opt Soc Am A 1986;3:1897–907.
[55] Schulz TJ, Snyder DL. Image recovery from correlations. J Opt Soc Am A 1992;9(8):1266–72.
[56] Fienup JR. Reconstruction of an object from the modulus of its Fourier transform. Opt Lett 1978;3:27–9.
[57] Fienup JR. Phase retrieval algorithms: a comparison. Appl Opt 1982;21:2758–69.
[58] Bates RHT. Fourier phase problem are uniquely solvable in more than one dimension I: underlying theory. Optik 1982;61:247–62.
[59] Garden KL, Bates RHT. Fourier phase problem are uniquely solvable in more than one dimension II: one dimensional considerations. Optik 1982;62:131–42.
[60] Fright WR, Bates RHT. Fourier phase problem are uniquely solvable in more than one dimension III: computational examples for two dimensions. Optik 1982;62:219–30.
[61] Sault RJ. Two procedures for phase estimation from visibility magnitudes. Aust J Phys 1984;37:209–29.
[62] Lane RG. Recovery of complex images from Fourier magnitudes. Opt Commun 1987;63(1):6–10.
[63] Sasaki O, Yamagami T. Phase retrieval algorithms for non-negative and finite-extent objects. J Opt Soc Am A 1987;4(4):720–6.
[64] Millane R. Phase retrieval in crystallography and optics. J Opt Soc Am A 1990;7(3):394–411.
[65] Pérez-Ilzarbe MJ, Nieto-Vesperinas M. Phase retrieval of photon-limited stellar images from information of the power spectrum only. J Opt Soc Am A 1991;8(6):908–18.
[66] Nieto-Vesperinas M. A Fortran routine to estimate a function of two variables from its autocorrelation. Comput Phys Commun 1993;78:211–7.
[67] Crimmins TR, Fienup JR, Thelen BJ. Improved bounds on object support from autocorrelation support and application to phase retrieval. Opt Soc Am A 1990;7(1):3–13.
[68] Brigham EO. The fast Fourier transform. Englewood Cliffs, NJ: Prentice-Hall; 1974.
[69] Gonzales RC, Wintz P. Digital image processing. USA: Addisson-Wesley; 1987.
[70] Gerchberg RW, Saxton WO. A practical algorithm for the determination of phase from image and diffraction plane pictures. Optik 1972;35:237–46.
[71] Saxton WO. Computer techniques for image processing in electron microscopy. New York: Academic Press; 1978.
[72] Pérez-Ilzarbe MJ, Nieto-Vesperinas N, Navarro R. Phase retrieval from experimental far-field intensity data. J Opt Soc Am A 1990;7(3):434–40.
[73] Matheron G. La théorie des variables régionalisées et ses applications, Fontainebleau: Les cahiers du centre de morphologie de Fontainebleau, Fascicule 5; 1970.
[74] Ehrlich R, Etris EL, Brumfield D, Yan LP, Crabtree SJ. Petrography and reservoir physics III: physical models for permeability and formation factor. Am Assoc Petroleum Geol Bull 1991;75(10):1579–92.
[75] Ehrlich R, Crabtree SJ, Horkowitz KO, Horkowitz JP. Petrography and reservoir physics I: objective classification of reservoir porosity. Am Assoc Petroleum Geol Bull 1991;75(10):1547–62.
[76] McCreesh CA, Ehrlich R, Crabtree SJ. Petrography and reservoir physics II: relating thin section porosity to capillary pressure curves, the association between pore types and throat size. Am Assoc Petroleum Geol Bull 1991;75(10):1563–78.
[77] Anguy Y, Ehrlich R, Prince CM, Riggert V, Bernard D. The sample support problem for permeability assessment in sandstone reservoirs. In: Yarus JM, Chambers RL, editors. Stochastic modeling and geostatistics, AAPG Computer Applications in Geology No. 3. Tulsa: American Association of Petroleum Geologists; 1994. p. 37–54.

[78] Prince CM, Ehrlich R, Anguy Y. Analysis of spatial order in sandstones II: grain clusters, packing flaws and the small-scale structure of sandstones. J Sediment Res A 1995;65(1):13–28.
[79] Graton LC, Fraser HJ. Systematic packing of spheres with particular relation to porosity and permeability. J Geol 1935;43:785–909.
[80] Berg RR. Capillary pressure in stratigraphic traps. Am Assoc Petroleum Geol Bull 1975;59(6):939–56.
[81] Anguy Y, Belin S, Bernard D, Fritz B, Ferm JB. Modeling physical properties of sandstone reservoirs by blending 2D image analysis data with 3D capillary pressure data. Phys Chem Earth A 1999;24(7):581–6.
[82] Rosenfeld A, Kak AC. Digital picture processing, vol. 1. New York: Academic Press; 1982.
[83] Blackman RB, Tukey JW. The measurement of power spectra. New York: Dover; 1958.
[84] Pérez-Ilzarbe MJ. Phase retrieval from the power spectrum of a periodic objet. J Opt Soc Am A 1992;9(12):2138–48.
[85] Sneddon INP. The use of integral transforms. New York: McGraw-Hill; 1972.
[86] Howell KB. Fourier transforms. In: Poularikas AD, editor. The Transforms and applications handbook; 1996. p. 95–225.
[87] Ferreol B, Rothman DH. Lattice-Boltzmann simulations of flow through Fontainebleau sandstone. Transp Porous Media 1995;20:3–20.
[88] Guéguen Y, Palciauska V. Introduction á la physique des roches. Paris: Hermann; 1992.